J. Fluid Mech. (1990), *vol.* 219, *pp.* 469–497
Printed in Great Britain

Transient features of natural convection in a cavity

By JOHN C. PATTERSON AND S. W. ARMFIELD
Centre for Water Research, University of Western Australia, Nedlands, W.A. 6009, Australia

(Received 7 August 1989 and in revised form 23 March 1990)

Comparisons of numerical and experimental results for transient two-dimensional natural convection initiated by instantaneously heating and cooling the opposing vertical walls of a square cavity containing a stationary and isothermal fluid are presented. The good comparisons indicate that the simulation is capturing the important features of the flow. Several features are identified and discussed in detail; in particular, the presence of travelling wave instabilities on the vertical-wall boundary layers and horizontal intrusions, the existence of a rapid flow divergence in the region of the outflow of the intrusions, and the presence of cavity-scale oscillations, caused by the interaction of the intrusions with the opposing vertical boundary layer. The utilization of both numerical and experimental investigations has allowed a more complete exploitation of the available resources than would have been possible had each been conducted separately.

1. Introduction

Natural convection driven by imposed horizontal density gradients finds many applications in engineering: horizontal transport in water bodies, reactor cooling systems, and crystal growth procedures to name but a few. In many of these and other applications, the forcing which provides the horizontal gradient is unsteady, and the response of the system to changing, and particularly to suddenly changing boundary conditions is of fundamental interest.

The most studied form of this problem is the case of a rectangular cavity with differentially heated sidewalls. The steady-state version of this problem has received considerable attention since Batchelor (1954) first addressed the case of heat transfer across double-glazed windows. Since then, a large body of literature examining various experimental, numerical and theoretical aspects has appeared. Much of this is summarized in the reviews by Catton (1978) and Ostrach (1982). In spite of the applications of the unsteady case, however, the imposition of unsteady boundary conditions was evidently not considered in any detail until Patterson & Imberger (1980) discussed the case of instantaneous heating and cooling of the opposing sidewalls.

In Patterson & Imberger (1980, hereinafter referred to as PI), a classification of the development of the flow through several transient flow regimes to one of three steady-state types of flow was devised. The classification depended on the relative values of the Rayleigh number Ra and various combinations of the Prandtl number Pr and the aspect ratio A, where

$$Ra = \frac{g\alpha\Delta T h^3}{\nu\kappa}, \tag{1}$$

$$Pr = \frac{\nu}{\kappa}, \tag{2}$$

$$A = \frac{h}{L}, \tag{3}$$

with g the acceleration due to gravity, α the coefficient of thermal expansion, ΔT the temperature difference between initial and boundary temperatures, h and L the cavity height and length respectively, ν the kinematic viscosity, and κ the thermal diffusivity. Several regimes were described: in particular, one regime ($Ra > Pr^4 A^{-4}$) approached steady state in an oscillatory manner, characterized by a decaying oscillation in the measure of the net heat transfer across the centreline of the cavity. The engineering applications of this unsteady heat transport are of some importance, particularly if the timescales of the flow development and of the oscillation are comparable to the forcing timescales.

Other numerical simulations separately reached a similar conclusion (for example, Gresho *et al.* 1980; Staehle & Hahne 1982) using different numerical schemes. The importance of the result to engineering applications led Yewell, Poulikakos & Bejan (1982) to mount an experiment to test for the presence of this oscillatory behaviour, in apparently the first experiment designed to investigate the transient part of the flow. Although the results did not show any evidence of the oscillatory behaviour, many other aspects of the PI classification were supported. However, as shown by Patterson (1984), the Yewell *et al.* experiments were in a regime in which oscillations were not expected, and their results were entirely consistent with the PI predictions for the regime actually achieved.

Ivey (1984) carried out a series of experiments again designed to test for the existence of the oscillatory behaviour. Here, the correct regime was selected, with a Rayleigh number of $O(10^9)$ and $Pr \sim 7$ in a cavity of aspect ratio 1, and evidence of the oscillations was expected. The results did not, however, show a clear indication of the expected behaviour: time series from several thermistors placed at various locations in the upper part of the cavity showed a degree of variability, but this was of much higher frequency than the first-mode internal wave activity predicted by PI, and appeared to be associated with the downstream behaviour of the horizontal intrusions from the corners, interpreted by Ivey as an internal hydraulic jump. Further, the results indicated several other interesting features of the flow. In particular, at an early stage of the flow development, Ivey reported that the core of the cavity was rotating in a direction counter to the boundary-driven flow; that is, with the hot wall to the right, the core rotated in a clockwise direction. In a flow in which convection dominates the heat transfer, such a reversal would have a substantial effect on the net heat transfer properties.

The numerical solutions of Chenoweth & Paolucci (1986) for a variety of steady problems with air as the working fluid were consistent in appearance with the Ivey concept of an internal hydraulic jump, and indeed they suggested that the jumps played an important role in the transition to turbulence. Paolucci & Chenoweth (1989) found numerical solutions for the transient flows generated from an initially steady flow at a particular Rayleigh number which was suddenly increased. These results also gave support to the Ivey conjectures with respect to the hydraulic jump and associated oscillatory behaviour. Wave activity at both high and low frequencies was observed, and associated with boundary-layer instabilities and internal waves. This activity was in the context of the initial background stratification inherent in the steady flow initial condition, and persisted for long integration times and in some cases was associated with the transition to turbulence. Thus although some information on the approach to steady state was available, including estimates of the

wave properties, the paper was more concerned with the transition from steady to unsteady flow, as a prelude to turbulence, than with the generation of a genuinely steady, laminar flow from an initially stationary, unstratified state. Consequently, many of the arguments of PI relating to flow development are not relevant to their simulations.

Paolucci & Chenoweth (1989) also briefly reported a simulation of the Ivey experiment, showing only temperature traces at two specific experimental locations. These were of similar character to the Ivey results, but did show evidence of the presence of low-frequency oscillations, consistent with the earlier numerical results. The paper also reported that the flow became oscillatory after a period of apparent steady-state behaviour. In particular, the wall boundary layers were reported as becoming unsteady following the decay of the low-frequency oscillations. Schladow, Patterson & Street (1989) performed more detailed numerical simulations of the Ivey experiment. Their results again showed the oscillatory behaviour in the net Nusselt number, and supported the conclusions of PI. There was no evidence of the reverse circulation observed by Ivey in the period of flow development, but they showed that the presence of a weak initial stratification in the cavity was sufficient to generate a reverse circulation consistent with the Ivey result. The numerical simulations did, however, show intrusion flow structures of the kind interpreted as hydraulic jumps, with qualitatively similar downstream behaviour. Schladow *et al.* discussed a number of possible mechanisms for the formation of the jump-like structures in addition to the Ivey argument, including one based on entrainment of the intrusion by the eddies which form in the interior corners.

The questions relating to the formation of these complex intrusion flow structures and the oscillations observed in the Nusselt number remained therefore largely unanswered. In this paper a joint experimental and numerical investigation is described which attempts to clarify these questions. Here, the results of an experiment at a Rayleigh number similar to that of the Ivey experiment are described. The experimental procedures are such that more attention is paid to the initiation of the experiment, and to the control of the initial stratification. Briefly, the results confirm that the reverse circulation in the core is not present but that the complex flow structures in the horizontal intrusions are present; the presence of a travelling wave in the intrusion is indicated; low-frequency oscillations are separately observed in the intrusion; and the presence of instabilities in the thermal boundary layer are observed on two separate occasions.

In parallel with the experimental program, a numerical investigation has also taken place. The development of a time-accurate second-order scheme is described, and the results compared with the experimental results at two levels. First, thermistor time series at a number of locations are compared with temperature time series at the corresponding simulation locations, including identification of the various instabilities present. Second, streak photographs from the experiment are directly compared with streamline plots from the simulations. The comparisons are excellent, and indicate that the numerical simulation is capturing the important processes in the flow development.

By making use of this combined experimental and computational investigation it has been possible to identify a number of flow features that have not been previously observed, with the experimental results giving confidence that they are not numerical effects. Thus, for instance, the occurrence of the boundary-layer instability in the context of the present problem or of intrusion splitting at the downstream end, both of which are discussed here, were not reported by Schladow *et al.* (1989). The

code used by Schladow *et al.* was similar to that used in the present investigation, although first order in time. In a recent paper, Schladow (1990) shows that by moving to a scheme of higher order in time these boundary-layer effects, reported by Patterson (1989), Armfield (1989), and discussed in the present paper, are captured. Schladow (1990) links the two groups of boundary-layer waves with the theoretical description of flow on a suddenly heated vertical plate (Brown & Riley 1973) and with the instabilities present on vertical heated plates (Gebhart & Mahajan 1982), and discusses the occurrence of the long-period waves in the context of the mechanisms suggested in P[T] and Schladow *et al.* (1989). It is of interest to note that, in the present investigation, the boundary layer instability was first observed in the numerical simulation, and was thought to be a spurious numerical effect. By using the numerical results to determine the placement of thermistors in the experimental apparatus, however, it was discovered that the simulation was accurately predicting a physical effect. The combined experimental and numerical investigation therefore allowed a more complete exploitation of the available resources than would have been the case were each branch conducted separately.

2. Experimental procedures

The only experiments undertaken with a view to examining the development of the flow from a stationary state were those of Yewell *et al.* (1982) and Ivey (1984). In the first case, the experiment was initiated by circulating pre-cooled fluid through a cooling jacket attached to the cold wall, and switching on electrical heaters embedded in the hot wall. The walls reached their operating temperatures in a time of O (15 min). Although this was short compared with the overall timescale of the experiment, it was not short compared with the timescale τ for the stabilization of the thermal boundary layer. From PI, this is given by

$$\tau \sim \frac{h^2}{\kappa Ra^{\frac{1}{2}}}. \tag{4}$$

For the Yewell *et al.* experiments, this was O (5 s). Thus even if the experiment had been in a regime in which the oscillatory behaviour was expected, it is not clear if the altered start-up conditions would have altered the conclusions. Ivey (1984) on the other hand, initiated the experiment by pouring pre-heated and pre-cooled water directly into water baths adjacent to the hot and cold walls. This procedure was completed in a time of O (5 s), substantially faster than the Yewell *et al.* procedure. From (4), the timescale for boundary-layer growth for the highest-Ra case dealt with by Ivey ($Ra \sim 1.2 \times 10^9$) is O (12 s), and although the start-up time was shorter than this, it was still comparable with the shortest timescale of the problem.

The present series of experiments was carried out in an apparatus designed to minimize the effects of a relatively slow initiation (see figure 1). The apparatus consists of a square cavity of side 24 cm and width 50 cm, the sidewalls, base, and top of which are constructed of 19 mm Perspex sheeting. The hot and cold walls are made of 1 mm copper sheet, braced on the outside with Perspex ribs. Insulated hot and cold water baths are separated from the copper walls by a 3 cm air gap, in which a sheet of polystyrene foam is placed during the setting up of the experiment. The bath walls facing the copper walls are pneumatically controlled gates which rise vertically. Thus, the baths are brought to the required temperatures, the foam sheet removed from the air gap, and the gates actuated. The heated and cooled water flood against

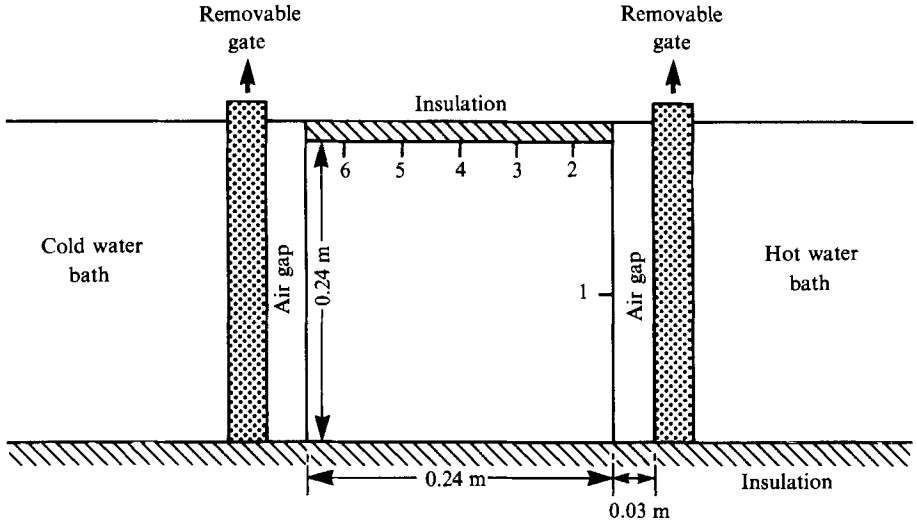

FIGURE 1. A schematic of the experimental apparatus. The numbers indicate the locations of the thermistors.

Thermistor number	x (cm)	y (cm)
1	23.8	12.0
2	19.0	22.5
3	15.5	22.5
4	12.0	22.5
5	8.5	22.5
6	5.0	22.5

TABLE 1. Thermistor locations, relative to the lower left corner of the cavity

the outside of the copper walls, achieving total contact in a fraction of a second. With a conduction timescale through the thin copper walls of order 10 ms, an initiation timescale of less than 1 s is achieved. The water baths are vigorously stirred to minimize boundary effects on the bath side of the copper walls, and the bath temperatures are maintained at their initial temperatures for the duration of the experiment. The cold bath is controlled by an immersion cooler operating at full capacity, with temperature control being achieved by a more powerful immersion heater. The hot bath is maintained by a similar heater. In both cases, temperature control within 0.05 °C was possible. By careful timing of the gate releases, suitable bracing of the supporting table, and bracing of the copper endwalls themselves, vibration was reduced to negligible amounts. The outside of the Perspex cavity walls, lid and base were lined with polystyrene foam for heat insulation. The insulation on one face was removable for photography.

Temperature time series were taken at the points 1–6 shown in figure 1, and in the hot and cold baths for control. The actual locations of the thermistor points are given in table 1. The thermistors were Thermometric FP07 fast response thermistors, connected to a 12 bit A-D board via a pre-amplifier, giving a resolution of 0.007 °C. The thermistors were mounted in thin, insulated tubing inserted through the lid of the cavity, placed away from the central plane so that simultaneous flow visualization was also possible. The thermistors were all sampled at 2 Hz, sufficiently

fast to resolve the highest expected frequencies, including that of the thermal boundary-layer instabilities, which, from Gebhart & Mahajan (1982), is of order 0.1Hz for the experimental parameter values.

Flow visualization was achieved with small rheoscopic particles (manufactured by Kalliroscope Corporation) of size approximately $6 \times 30 \times 0.07$ μm (e.g. Ivey 1984; Rhee, Koseff & Street 1984). These were illuminated by a sheet of light in the central plane of the cavity. The light sheet was formed by focusing light from an ordinary slide projector via an angled mirror below the cavity into a 1 cm wide non-reflecting channel directed into the bottom of the cavity. The interior of the cavity lid was coated with non-reflecting paint to minimize internal reflections. Streak photographs were taken using Ilford XP1-400 monochrome film, at f11.0. Usually, 8 s exposures were taken, although longer exposures were used in the later parts of the experiments. The nature of the particles is such that they align their larger dimension in the direction of the shear, and for this reason the streak photographs are not suitable as a means of determining velocity. However, the streak photographs give an integrated picture of the flow field over the period of the exposure. At no stage were three-dimensional motions observed in the central plane of the cavity.

The results reported here are for an end-to-end temperature difference of 4 °C ($\Delta T = 2$ °C), using water as the working fluid, yielding a Rayleigh number of 3.26×10^8, with a Prandtl number of 7.5, at an ambient temperature $T_0 = 18.25$ °C. This was sufficiently close to the Ivey (1984) experimental value for comparison of the main features; certainly both experiments fall in the same range of the PI scaling. From (4), the boundary-layer timescale is O (23 s).

3. Numerical procedures

3.1. *Formulation*

The experimental set-up is modelled by a square two-dimensional cavity of side h, containing a Newtonian fluid initially at rest and at temperature T_0. The upper and lower boundaries are insulated, and at time $t = 0$, the left- and right-hand endwalls are instantaneously cooled and heated to $T_0 - \Delta T$ and $T_0 + \Delta T$ and maintained at those temperatures thereafter. The subsequent motion is described by the usual equations, in which the Boussinesq assumption has been made,

$$u_t + uu_x + vu_y = -p_x + u_{xx} + u_{yy}, \tag{5}$$

$$v_t + uv_x + vv_y = -p_y + v_{xx} + v_{yy} + \frac{Ra}{Pr} T, \tag{6}$$

$$u_x + v_y = 0, \tag{7}$$

$$T_t + uT_x + vT_y = \frac{1}{Pr}(T_{xx} + T_{yy}), \tag{8}$$

where subscripts denote partial differentiation, u and v are the velocity components in the x- and y-directions, T is the temperature, and the other terms are defined in §1. In (5)–(8), u and v have been non-dimensionalized with respect to ν/h, x and y with respect to h, and $T - T_0$ with respect to ΔT.

The boundary conditions are given by

$$u = v = 0, \quad T = 0 \quad \text{at all} \quad x, y \quad \text{and} \quad t < 0, \tag{9}$$

$$u = v = 0 \quad \text{on} \quad x = 0, 1; \quad y = 0, 1, \tag{10}$$

$$\frac{\partial T}{\partial y} = 0 \quad \text{on} \quad y = 0, 1, \tag{11}$$

$$T = \pm 1 \quad \text{on} \quad x = 0, 1 \quad \text{for} \quad t \geqslant 0. \tag{12}$$

3.2. *Discretization*

Because of the large variation in lengthscales in this problem it is necessary to use a mesh that concentrates points in the boundary layer and is relatively coarse in the interior. The mesh used here is such that the point near a vertical wall is located one thousandth of a cavity width in from the wall, with the mesh then expanding at a rate of 10% until the edge of the thermal boundary layer is reached. From PI, the thermal boundary-layer thickness scale is given by

$$\delta_T \sim \frac{h}{Ra^{\frac{1}{4}}}, \tag{13}$$

which for this case gives a non-dimensional thickness estimate of 0.007. With the point nearest to the wall located 0.001 of the cavity width from the wall this procedure places about five mesh points in the thermal boundary layer. This results in a grid composed of 80×80 points. Variables are stored at staggered locations in the conventional manner used with SIMPLE schemes (Patankar 1980); that is, pressure and temperature are stored at the same locations on the base grid, whilst the velocity storage locations are offset half a mesh width in their respective directions from the base grid.

On this mesh the derivative terms are discretized in the following manner. Using finite volumes all second derivatives are approximated by second-order central differences as, typically,

$$T_{xx}(x^i, y^j) = \frac{\left[\dfrac{T^{i+1} - T^i}{\Delta x^{i+1}} - \dfrac{T^i - T^{i-1}}{\Delta x^i}\right]^j}{\frac{1}{2}[\Delta x^{i+1} + \Delta x^i]} + O(\Delta x^2), \tag{14}$$

where $\Delta x^i = x^i - x^{i-1}$, x^i is the x location of the ith mesh point, T^i is the approximation for T at the associated mesh point, and $\Delta x^2 = \Delta x \, \Delta x$. First derivatives occurring in the convective terms are approximated by a QUICK scheme (Leonard 1979).

Use of a non-constant mesh with differencing as defined above can lead to an inaccuracy due to the change in adjacent meshes (Patterson 1983). In the present case, the limitation of the maximum change in spacing between adjacent nodes to 10% of the mesh size ensures that the solution is not degraded by this effect.

The discretization produces the usual fringed block tridiagonal matrix equation, one for each of the momentum, temperature and pressure equations. These equations are solved using an implicit alternating-direction Gauss–Seidel iterative method. Initially an estimate for the unknown quantity is obtained by making a linear extrapolation from the two previous time steps. This method has been found to reduce computation time by a factor of approximately two, relative to the method of using only the previous step value as an initial estimate. In each direction at each sweep location the differencing scheme used leads to the inversion of tridiagonal matrices, which is done using the simple and efficient Thomas algorithm. The SIMPLE scheme necessitates the use of under-relaxation for the correction to the stored pressure. In the present case a value of 0.8 has been used.

Various enhancements have been tested such as the SIMPLE-derived algorithms, PRIME (Maliska & Raithby 1983), PISO (Issa 1983) and SIMPLEC (Van Doormal &

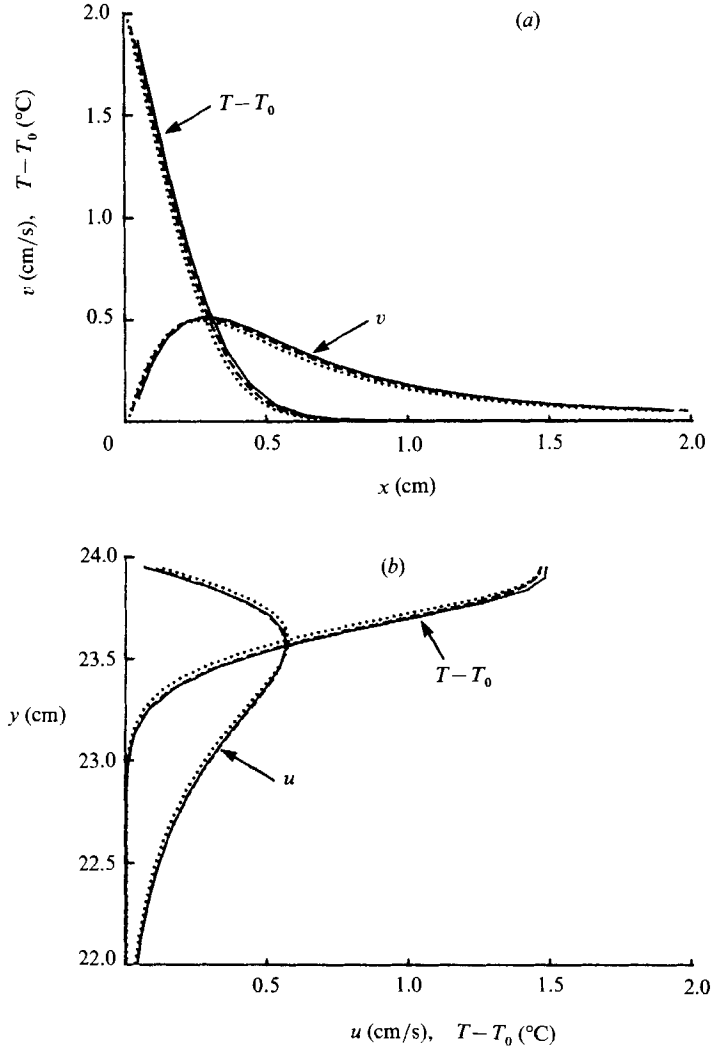

FIGURE 2. (*a*) Comparison of the results from the 80 × 80 standard mesh (solid line), 120 × 120 mesh (dashed line) and 150 × 150 mesh (dotted line) for the horizontal profiles of vertical velocity and temperature at mid-depth $y = 12$ cm, and $t = 142$ s. (*b*) Comparison of the results from the 80 × 80 standard mesh (solid line), 120 × 120 mesh (dashed line) and 150 × 150 mesh (dotted line) for the vertical profiles of horizontal velocity and temperature across the hot intrusion, at a location 2 cm in from the hot wall, and $t = 142$ s.

Raithby 1984), as well as alternative matrix solvers including the Cholesky preconditioned conjugate gradient method (Jackson & Robinson 1985). These strategies gave some improvement in the performance of this code without affecting the accuracy. Other forms of the code may provide more substantial improvements in performance (Kightly 1986; Perng & Street 1990). However, all results presented were obtained with the basic code described here.

3.3. *Time integration*

The time integration scheme is a second-order Crank–Nicholson predictor-corrector method in which the solution of the transport equations is carried out in the following order. First, all variables are known at time $t = n\Delta t$, where Δt is the time

step. Second, the heat equation (8) is inverted to obtain T^{n+1}, and using this value, the two momentum equations (5) and (6) are inverted, using an estimated pressure field to obtain a first approximation to u^{n+1} and v^{n+1}. A pressure correction equation, derived to enforce continuity (7), is then solved, and the pressure field adjusted. Finally, new estimates of u^{n+1} and v^{n+1} are calculated. This procedure is repeated until a preset sup-norm convergence criterion is met. The non-dimensional time step Δt was determined by numerical experiment to be sufficiently small so that the time-wise oscillations that can occur with Crank–Nicholson schemes were not present. The resulting value was $\Delta t = 1.25 \times 10^{-5}$, corresponding to, in dimensional terms, 0.7125 s for simulation of the experimental conditions.

3.4. *Grid independence*

To test the grid independence of the scheme the solution has been obtained on the mesh defined above and on two additional fine meshes, with the following parameters. The first mesh has one quarter of the step size at the wall, the same grid expansion factor, and one quarter of the time step of the standard mesh. This gives a grid of 120×120 with approximately the same grid spacing in the core. The second mesh has one half the step size at the wall, one half the grid expansion function (i.e. an expansion rate of 5%), and one quarter of the time step of the standard mesh. This gives a grid of 150×150 points with approximately one half of the standard grid spacing in the core. Figure 2(*a*) shows the vertical velocity and temperature profiles as a function of horizontal distance from the hot wall at midheight in the thermal boundary layer. The horizontal velocity and temperature profiles as a function of height in the upper part of the cavity in the outflow corner region (2.0 cm from the hot wall) are shown in figure 2(*b*). Both figures are for $t = 142$ s, after the thermal boundary layer is established and the intrusion has passed the 2 cm point. In both cases, the variation between the three representations is small, indicating that the standard mesh is free of grid- and time-step-dependent errors.

4. Results

In this section the results of both the experimental and numerical aspects are reported. The emphasis here is on a qualitative description of the flow and the comparison between the numerical and experimental results. The comparisons are carried out in two ways. First, thermistor traces are compared with the predicted temperature signal at the same location, and second, the streak photographs are compared with streamline plots drawn from the simulation results.

4.1. *Thermistor time series*

Figure 3 shows the measured temperature in the form $T - T_0$ from thermistor 1. The thermistor was located at midheight and with the tip 2 mm in from the hot wall; from (13), the thermal boundary-layer thickness scale is expected to be of order 1.8 mm, and the thermistor was therefore expected to capture the events on the outer boundary of the layer. However, the physical size of the thermistor bead is of approximately 1.5 mm, and the signal is integrated over this region.

There are several aspects of interest immediately evident from the experimental result. First, the thermistor does not respond until 4 s has elapsed, corresponding to the thermal boundary layer growing into the cavity. For a short time after initiation, convection will play a small role, and the signal at the thermistor location will primarily be determined by the conduction of heat in from the boundary. The

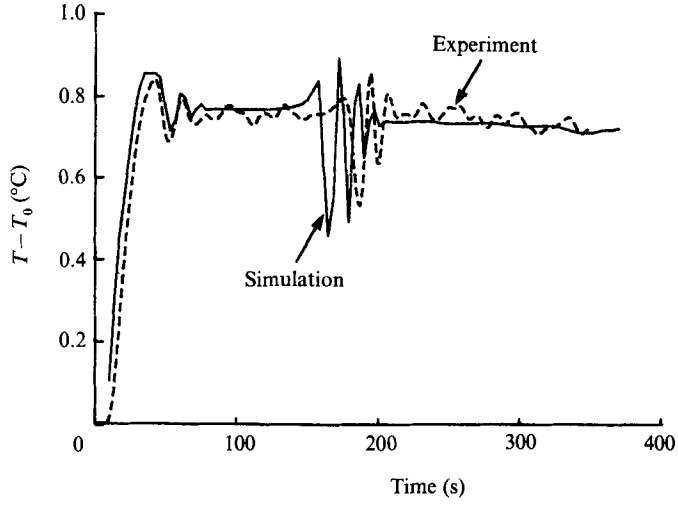

FIGURE 3. The measured (broken line) and computed (solid line) temperature at the location of thermistor 1 in the hot-wall thermal boundary layer, as a function of time.

solution for the equivalent semi-infinite bar impulsively heated at one end is given by Carslaw & Jaeger (1959) and, for the present parameter values, suggests that, at 2 mm, a value of $(T-T_0)/\Delta T$ of 0.007 should be achieved in 2.0 s. At 3 mm, however, the predicted response time for a 0.007 signal is 4.5 s. The response is clearly extremely sensitive to the actual location and small errors of a fraction of a mm in the location of this thermistor will therefore influence strongly the predicted response time. Further, the integrated nature of the signal and convection slow down the measured response at the inner location. The indication is therefore that the boundary layer is responding as expected to an instantaneous change in temperature and that the initiation time is small. Second, the growth of the temperature signal after response follows an approximately exponential growth, but slower than that expected from a pure conduction solution, as expected for a conduction-dominated but convection-influenced process. Third, following the initial period of growth, the signal becomes approximately steady, with the exception of two distinct disturbances, corresponding to the steady-state boundary-layer model of PI. This is achieved in a timescale of order 40 s, compared with the prediction of 23 s suggested by (4). There are two clear modifications to the steady signal, the first at $t \sim 40$ s, and the second at $t \sim 160$ s. These perturbations will be discussed in more detail below. Apart from these perturbations the boundary layer is substantially steady after the period of initial growth, supporting the PI model of a thermal boundary layer initially governed by a balance between temperature growth and conduction from the wall, followed by a balance between vertical convection and conduction from the wall. As noted above, the thermistor is actually located outside the thermal boundary-layer scale with the result that the achieved steady value of $(T-T_0)$ is 40% of ΔT. Only the first 300 s of the record are shown; no substantial changes are evident in the remainder. As will be shown below, there is evidence of a low-frequency oscillation (of period O (70 s)) in the later part of the record. There is no evidence from either the experimental or numerical results of the development of wall boundary-layer unsteadiness at times beyond O (1000 s) as briefly reported by Paolucci & Chenoweth (1989). This inconsistency may be due to the slightly lower Ra value used here.

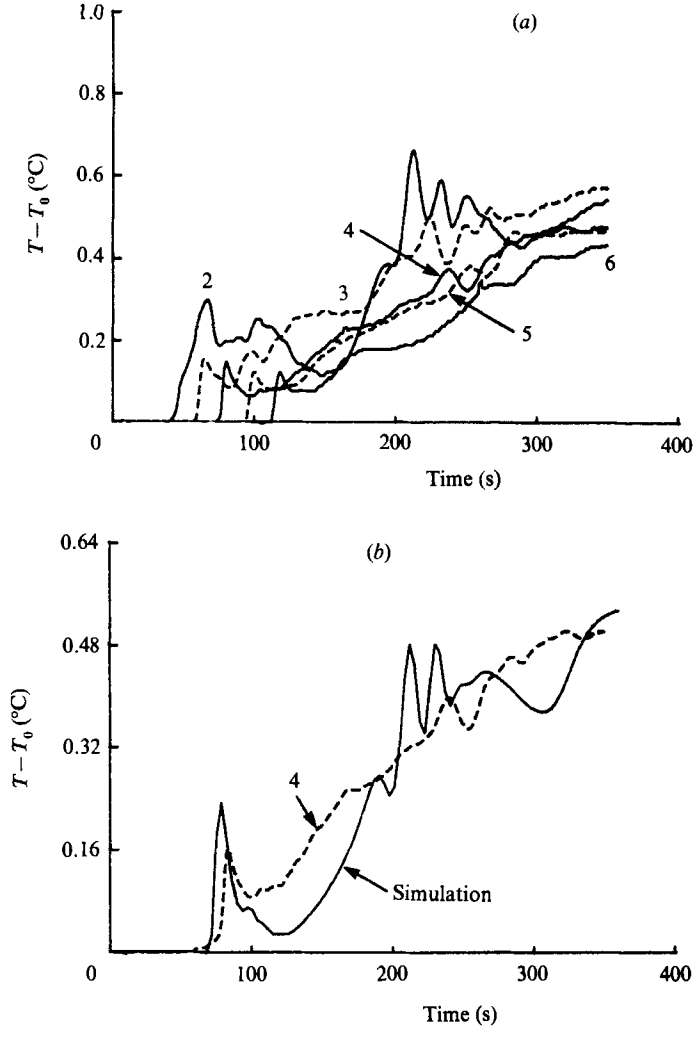

FIGURE 4. (*a*) The measured temperatures at thermistor locations 2–6 as marked in the heated intrusion, as a function of time. (*b*) The measured (broken line) and simulated (solid line) temperatures at thermistor location 4 (the midpoint of the cavity width), as a function of time.

Also on figure 3 is the simulated temperature at the same height and at 2.5 mm in from the wall. The mean steady temperature is initially slightly higher than the observed value; however, the extreme sensitivity to horizontal location in this region of high temperature gradient means that a change of a fraction of a mm in either location would account for this. The features of the observed signal are exceptionally well reproduced, with the exception that the numerical result appears to respond slightly faster, and in general leads the experimental result with the second group of instabilities occurring some 20 s earlier in the numerical result. This time offset is consistent with the experiment achieving a slightly lower Rayleigh number than intended, perhaps through boundary effects in the water baths. Alternatively, minor heat losses may account for the lagged experimental result. These aspects have not been pursued as the numerical simulation is clearly reproducing the features of the experiment. The amplitude of the perturbations is slightly greater than that

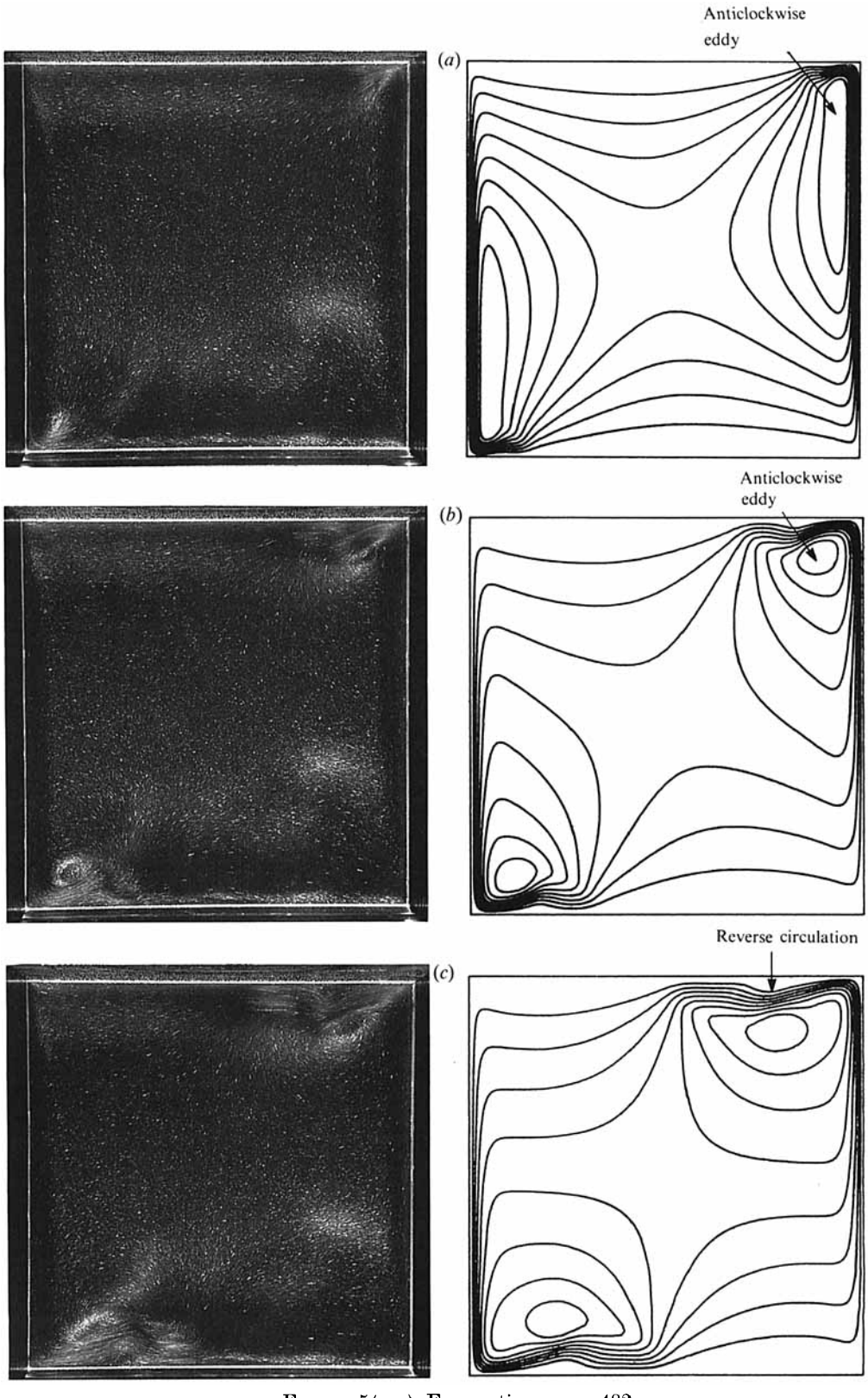

FIGURE 5(*a–c*). For caption see p. 482.

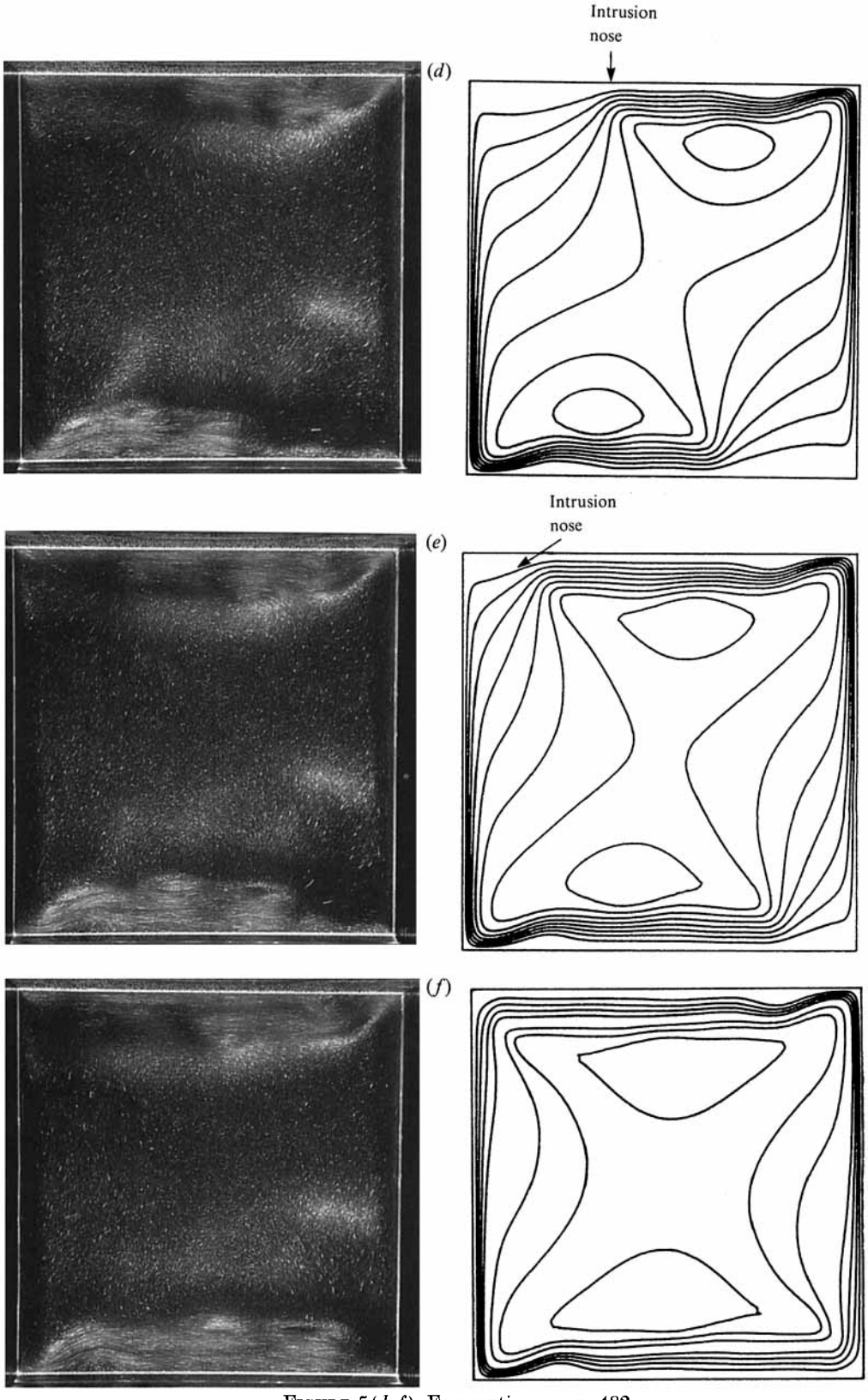

FIGURE 5(*d–f*). For caption see p. 482.

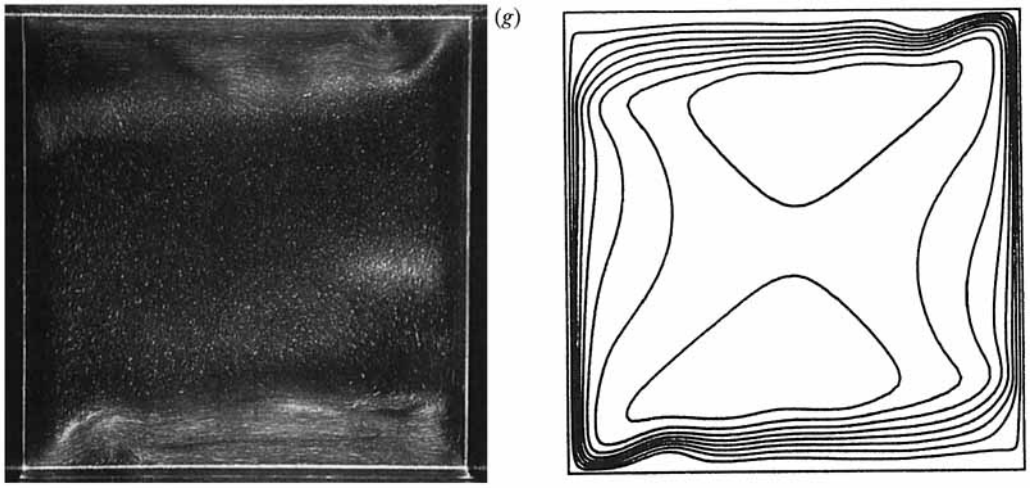

FIGURE 5. The streak photographs and simulated streamlines at various times after initiation. The streak photographs are 8 s exposures, beginning at the times indicated. The maximum value of the stream function ψ is also given in each case, and eight contours are drawn between the zero and maximum values of ψ. (*a*) 32 s, $\psi_{max} = 5.9 \times 10^{-4}$ m^2 s^{-1}; (*b*) 48 s, $\psi_{max} = 1.1 \times 10^{-3}$ m^2 s^{-1}; (*c*) 64 s, $\psi_{max} = 1.2 \times 10^{-3}$ m^2 s^{-1}; (*d*) 80 s, $\psi_{max} = 1.25 \times 10^{-3}$ m^2 s^{-1}; (*e*) 96 s, $\psi_{max} = 1.25 \times 10^{-3}$ m^2 s^{-1}; (*f*) 112 s, $\psi_{max} = 1.24 \times 10^{-3}$ m^2 s^{-1}; (*g*) 128 s, $\psi_{max} = 7.2 \times 10^{-4}$ m^2 s^{-1}.

observed; again these characteristics are extremely sensitive to the location of the reference point. The numerical results are similar in character to those of Schladow (1990); the different Ra value and the different reporting locations, however, preclude a direct comparison.

The time series from the thermistors at locations 2–6 are shown in figure 4(*a*). These thermistors are all located 15 mm below the lid of the cavity, and at horizontal positions 50 mm, 85 mm, 120 mm, 155 mm, and 190 mm from the hot wall (table 1). The increase in temperature for each thermistor is an indication of the passage of the nose of the heated intrusion, allowing an estimate of the speed of the nose to be calculated as 2 mm s^{-1}. Following PI, the intrusion will be governed by a viscous–buoyancy balance, since a purely inertial intrusion cannot exist unless $Ra > Pr^{16}A^{-12}$, which is not the case here. The PI scaling yields, for a viscous intrusion, a velocity of order 3 mm s^{-1}, consistent with the measured result. The rise in temperature is followed immediately by a drop as the nose of the intrusion passes by. Thermistors 2, 3, and 4 (near the hot wall) show evidence of an oscillation beginning at around 80 s; this is evidently the perturbation observed on the thermal boundary layer at 40 s which has travelled up the layer and along the intrusion. Similarly, at 200 s, all thermistors except thermistor 6 show a strong oscillatory signal which is the effect of the second thermal boundary-layer perturbation observed at 160 s, shown in figure 3. Using the intrusion velocity of 2 mm s^{-1} calculated above and noting the times that the intrusion passes each thermistor location, it may be estimated that the intrusion reaches the far wall at time 139 s. This implies that the cold intrusion reaches the base of the hot-wall thermal boundary layer at 139 s, triggers a perturbation that travels up the vertical layer, becoming evident at the midheight at time 160 s, and travels along the intrusion at reduced speed with decaying amplitude. Thus each of thermistors 2–6 shows the instability with decreasing amplitude, with the effect being totally dissipated by the time thermistor 6 is reached. Since the perturbation travels from the base of the thermal boundary layer to the midheight (12 cm) in 21 s, its speed in the vertical layer may be estimated as

0.6 cm s^{-1}; in the horizontal intrusion the amplitude increases substantially and the speed drops to 2.5 mm s^{-1}, based on the times of appearance in each thermistor signal. The perturbation velocity is, however, greater than the intrusion speed of 2 mm s^{-1}. This result is consistent with the non-appearance of the first perturbation in the signal from thermistor 6 as noted above; the perturbation reaches the nose of the intrusion before thermistor 6 is reached. The relative speed of the perturbation to the intrusion implies that the local internal Froude number is less than one, which has implications with respect to the character of the intrusion itself, as discussed below. This mechanism for the triggering of the second group of instabilities was also suggested by Schladow (1990) from numerical results, although explicit results for wave speeds were not discussed.

Figure 4(*b*) shows the simulated and observed temperature time series at the location of thermistor 4 (on the centreline of the tank). The comparison here is not as good as in the thermal boundary layer; however, the simulated results display the same general features. Again, the predicted instability occurs earlier than the observed, and is of higher amplitude. This is a region of high vertical gradient, and the comments above with respect to location are also relevant here.

4.2. *Flow field*

On a broader scale of comparison, computed streamlines and the observed streaks are compared in figures 5 and 6 for a range of times from near initiation to near steady state. The selection of times also allows a description of the flow evolution and the comparisons shown are typical of those obtained at all stages. The streaks are 8 s exposures, with the exception of figure 6(*e*) which is over 24 s, and the streamlines are at the nearest available time to the initial time of the streaks. In each streamline plot, eight equally spaced streamlines between, but not including, the minimum value (zero, on the boundary) and the maximum value of the stream function are drawn. The maximum value of a stream function in dimensional units is indicated in each figure legend. In all cases the hot wall is on the right, and reference is made to the hot wall and the heated intrusion in the following description. For clarity, the locations of the features of the flow discussed below are shown only on the streamline plots.

Figure 5(*a–g*) shows the development of the flow after establishment of the thermal boundary layer, beginning at an elapsed time of 32 s (5*a*) and ending at 128 s (5*g*). This sequence shows the formation of an anticlockwise eddy in the corner, below the intrusion (5*a*, *b*). The intrusion separates from the horizontal wall (5*b*), and a small reverse circulation is set up between the intrusion and the wall (5*c*). The intrusion nose penetrates to about the half-width position by 80 s (5*d*), and the eddy formerly in the corner has been advected towards the far wall, but at a slower rate than the intrusion speed. The separation has remained in approximately the same location. By 96 s (5*e*), the intrusion has reached approximately two thirds of the cavity width, at 112 s (5*f*) the intrusion has almost reached the far wall and the eddy is at mid-distance, and at 128 s (5*g*), the intrusion has reached the far wall. These times are consistent with the indicators from the thermistor signals shown in figure 4(*a*).

The streamline plots generated by the simulation show essentially the same patterns as the streaklines. Quantitative comparisons are not possible as the streaklines are not good indicators of velocity. As noted above, however, they do indicate the flow direction locally. In every case, the numerical results have reproduced the features of the observations.

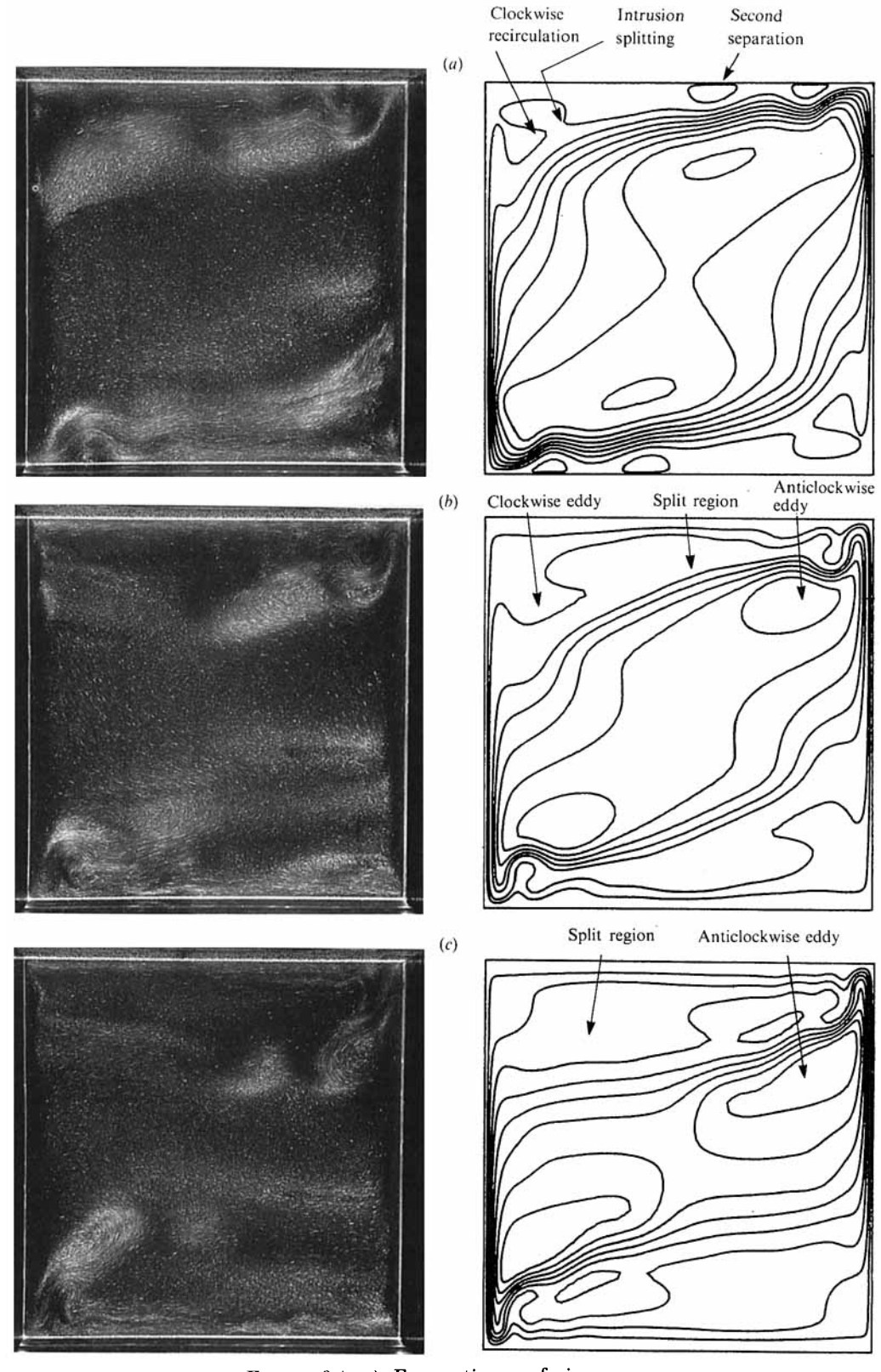

FIGURE 6 (*a–c*). For caption see facing page.

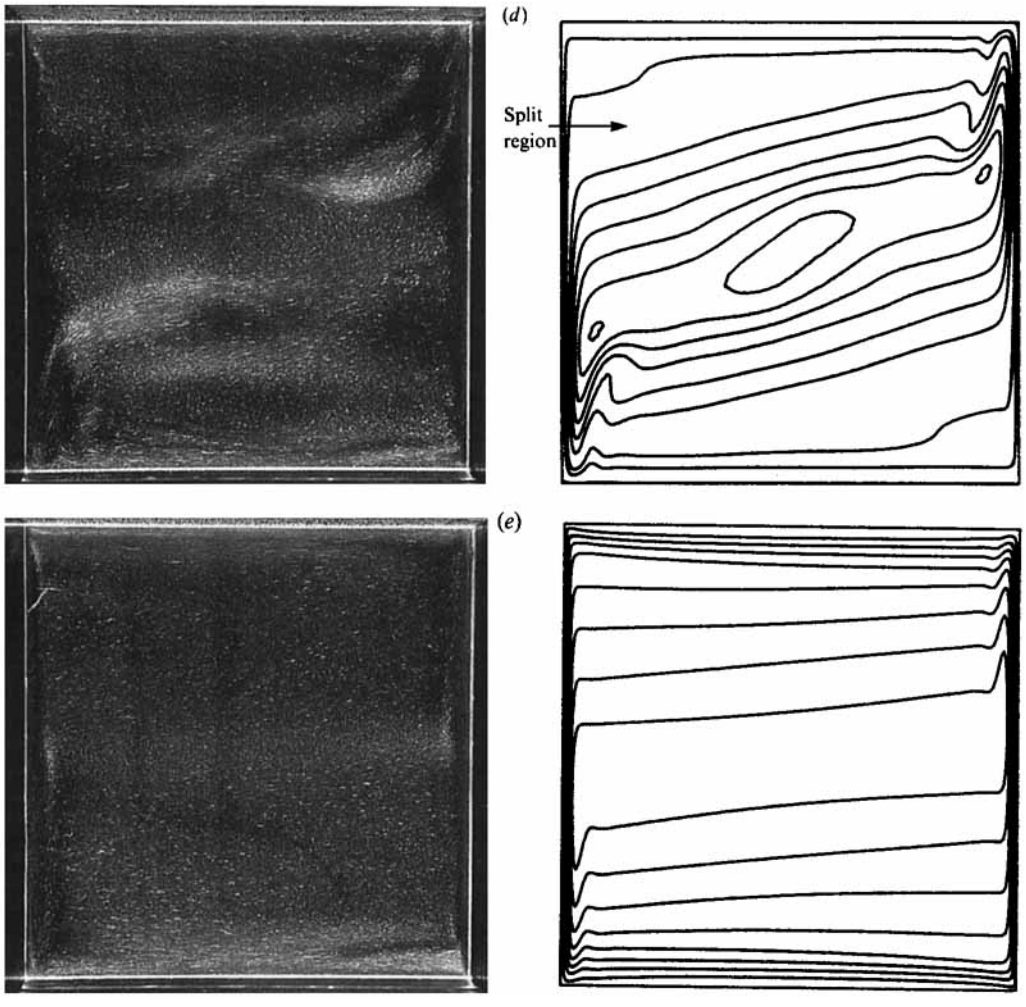

FIGURE 6. As for figure 5, at a later stage of the flow, with (*e*) being exposed over 24 s. (*a*) 176 s, $\psi_{max} = 1.0 \times 10^{-3}$ m^2 s^{-1}; (*b*) 256 s, $\psi_{max} = 9.0 \times 10^{-4}$ m^2 s^{-1}; (*c*) 352 s, $\psi_{max} = 7.5 \times 10^{-4}$ m^2 s^{-1}; (*d*) 480 s, $\psi_{max} = 6.3 \times 10^{-4}$ m^2 s^{-1}; (*e*) 1500 s, $\psi_{max} = 2.6 \times 10^{-4}$ m^2 s^{-1}.

The second group of observations (figure 6) follows the development of the motion after the first passage of the intrusion. The timing of the figures is more widely spaced in this case to allow the development to near steady state to be observed. Figure 6(*a*) (176 s) shows that the intrusion has split at the cold wall into two distinct streams: one, the hottest fluid, travelling along the cavity lid, and the other diverging towards the centre of the cavity, forcing the anticlockwise eddy back towards the hot wall. Some clockwise recirculation in the split region is evident, and the flow divergence near the emergent corner has become sharper. A second separation has formed just downstream of the first, possibly associated with the instability observed at this time in figure 4. At 256 s (6*b*), the split in the intrusion has penetrated back to the divergence and the anticlockwise eddy has been intensified. The weak clockwise circulation in the split region has remained located near the cold-wall end of the intrusion. This circulation is also clearly shown in enlarged form in figure 14, as discussed below. The divergence ahead of the intrusion separation is extremely

sharp, but the second separation has virtually disappeared. By 352 s (6*c*), the anticlockwise eddy has begun migrating into the core region, the interior of the cavity is being filled by the separated intrusion, and the sharpness of the diverging flow is retained. The remainder of the flow follows this pattern; the eddy moves progressively into the core until it meets with its equivalent cold-wall eddy to form a transient circulation in the centre, with the core being filled by means of the interior stream of the intrusion. A weak clockwise circulation maintains the two intrusion streams (6*d*, 480 s). The layering by the intrusion ultimately fills the cavity, the interior eddy and the clockwise eddy are dissipated, and the flow becomes essentially parallel in the core (6*e*, 1500 s). This streak photograph shows evidence of vertical flow reversal as the upper half of the vertical boundary layer detrains; the lower-half core flow remains essentially parallel as it is entrained. This streak photograph is taken over 24 s, indicating that the flow in the core is of substantially reduced velocity. Although the flow is not at steady state at 1500 s, the character does not change and no further streak photographs are shown.

The corresponding streamlines from the numerical result again compare well with the observations. The exception is in the direction of the flow of the fluid being entrained by the vertical boundary layers in figure 6(*b*). The observations indicate that the clockwise eddy at the upper end of the cold wall and the anticlockwise eddy at the lower end are stronger than that indicated by the simulation. This has the effect of returning the fluid from the interior cold intrusion back to the cold wall for entrainment, rather than across to the hot wall as indicated by the simulation. This is a transient effect and the difference quickly disappears; this is a region of extremely weak stratification and relatively low velocities, and small errors are acceptable.

5. Discussion

Although the experimental and numerical results confirm the extreme complexity of the flow development, it is possible to identify several distinct features which partly characterize the description. These are the presence of the perturbations on both the thermal boundary layer and the horizontal intrusions and the complex horizontal intrusion flow incorporating both the sudden divergence near the emerging corner and the subsequent intrusion splitting at the downstream end. In addition, the questions relating to the reverse core rotation and low-frequency oscillation in the Nusselt number remain. These latter questions are dealt with first.

There is no evidence in either the experimental or numerical results of the transient reverse rotation in the core reported by Ivey (1984). This was first reported at 80 s after initiation by Ivey, corresponding to figure 5(*d*), which shows no indication of such a centrally rotating eddy. This is consistent with the conclusion of Schladow *et al.* (1989) whose numerical results suggested that the reverse rotation was the result of a weak initial stratification in the cavity. Whilst this has implications for other flows and applications of a geophysical nature particularly, the matter is not pursued further here.

The oscillatory approach to steady state documented by a number of numerical investigations is also found here. As noted in the introduction, the computed Nusselt number at the wall Nu_W, and at the centreline of the cavity Nu_C, integrated over the depth, defined by

$$Nu = \frac{1}{2A}\int_0^1 \left[Pr\, uT - \frac{\partial T}{\partial x}\right]_X \mathrm{d}y \tag{15}$$

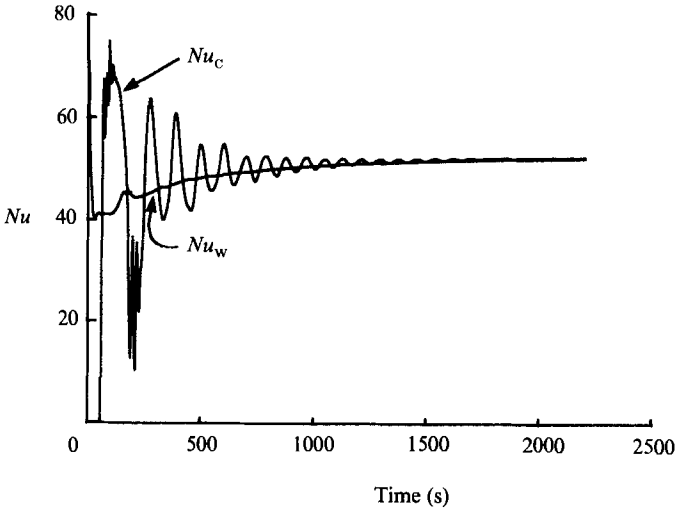

FIGURE 7. The computed Nusselt numbers at the wall (Nu_W) and at the centreline of the cavity (Nu_C), as a function of time.

where $X = 0$ for Nu_W and $X = \frac{1}{2}$ for Nu_C, have been commonly used as an indicator of the approach to steady state (e.g. PI; Gresho *et al.* 1980; Staehle & Hahne 1982; Schladow *et al.* 1989; Schladow 1990). Figure 7 shows a clear decaying oscillatory approach to steady state in Nu_C, with a period ranging from 87 s for the first cycle, to 60 s at $t \sim 1500$ s. There are also high-frequency signals present on both Nu_W and Nu_C during the first cycle. In the case of Nu_W, these are consistent with the passage of the perturbations on the thermal boundary layer referred to above, and reference to figure 3 shows that, on both occurrences, the appearance of the perturbations at mid-depth in the simulation result corresponds closely to the appearance of the high-frequency signal in the integrated result, expressed as Nu_W. Similarly, the high-frequency signals in Nu_C are the result of these perturbations travelling across the intrusion. While it is possible that other local oscillatory effects may be masked in the integration procedure, the integrated result is a clear indicator of the presence and subsequent decay of the cavity-scale waves, and of the presence of the two separate groups of boundary-layer instabilities.

The experimental results give a weaker indication of the oscillatory behaviour. The temperatures measured in the intrusion are strongly influenced by the passage of the perturbations, and it is not until these have passed that any indication of the presence of oscillatory behaviour is observed. Figure 8 shows the difference between the temperatures at locations 3 and 5 as a function of time, for the period 300–600 s. All activity from the boundary-layer perturbations has passed in this period, and a small-amplitude wave, of period approximately 70 s, is present. Although not definitive, this is a strong indication of the presence of a first-mode internal wave. The PI prediction for the period, based on a linear stratification, is O (55 s), consistent with the longer-timescale simulated result, although somewhat shorter than the measured and early-timescale simulated result. This discrepancy is likely to be due to the nonlinear nature of the stratification, particularly in the early part of the flow development.

The presence of the perturbations on the thermal boundary layer and subsequently on the horizontal intrusion is of considerable interest. These perturbations are triggered by a disturbance of the layer, in the first case by its initiation, and in the

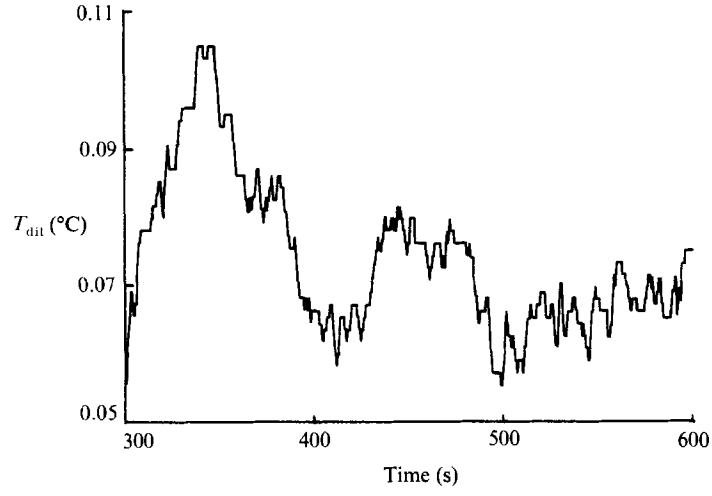

FIGURE 8. The measured temperature difference T_{dif} between thermistors 3 and 5, as a function of time after the initial transients have disappeared.

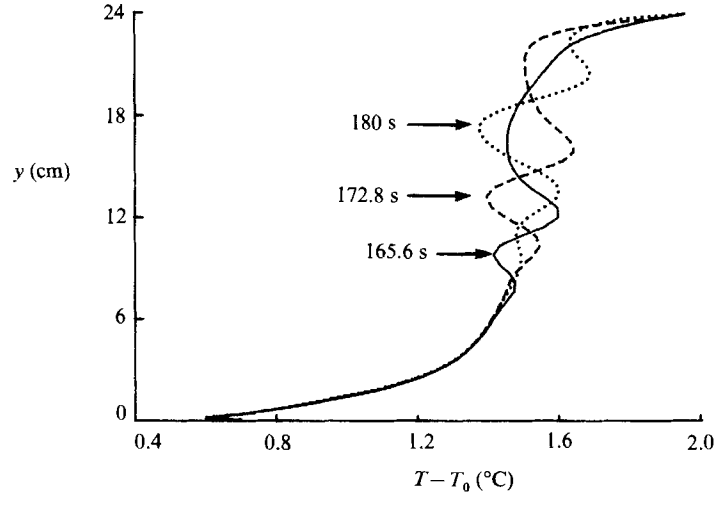

FIGURE 9. Computed vertical temperature profiles 1 mm in from the hot wall at t = 165.6 s, 172.8 s, and 180 s, as shown. The time label in each case identifies the second perturbation in the signal.

second case by the impact of the incoming intrusion. On the boundary layer, these perturbations result in travelling wave instabilities, increasing in amplitude in the direction of travel up the hot wall. Figure 9 shows, from the simulation, overlaid vertical temperature profiles in the thermal boundary layer (at a location 1 mm in from the hot wall) at times t = 165.6 s, 172.8 s and 180 s, corresponding to the time at which the second group of waves is travelling up the boundary layer. In each case the peak of a particular perturbation is marked. Clearly the amplitude of the perturbation is increasing as it moves up the boundary layer. The instability travels at a speed of 0.49 cm s^{-1}, compared with the mean boundary-layer velocity at mid-depth of 0.26 cm s^{-1} and peak velocity of 0.46 cm s^{-1}, and the experimental estimate of 0.6 cm s^{-1}. On the other hand, the experimental results suggest that the horizontal intrusion is stable to these perturbations, as the amplitude decreases with travel

along the intrusion as discussed above. The numerical results confirm that the amplitude of the perturbation dies away in the intrusion; the situation, however, is complicated by the presence of the rapid flow divergence near the emergent corner, and the specific results are not shown. It is evident, however, that, on the boundary layer, the perturbations are unstable and grow with passage; on the intrusion, the perturbations are stable, and decay before the far endwall is reached. The frequency of the travelling waves is observed to be 0.083 Hz, close to the 0.1 Hz estimate from Gebhart & Mahajan (1982) noted above.

These perturbations in the context of the present problem were reported by Patterson (1989) and Armfield (1989). Schladow (1990) related the presence of the first group of perturbations on the thermal boundary layer to the travelling 'leading-edge' effect discussed by Brown & Riley (1973) and others. In particular, on initiation, the effect travels upstream from the leading edge, in this case the lower corner of the heated plate, and manifests itself as the first travelling wave group observed. According to Brown & Riley, downstream (i.e. ahead) of the effect of the thermal layer is governed purely by horizontal conduction and vertical convection plays no role in the heat transfer. Convective heat transfer at a point commences only once the travelling waves have passed that point. Thus upstream of the waves the boundary layer is strongly influenced by vertical convection of heat and the approach to a steady state can begin. This is discussed at length by Schladow (1990) and further discussion is not warranted here; however, this description implies that the scales of the starting transient are those of the travelling waves observed.

Bergholz (1978) carried out a linear stability analysis on the steady flow between differentially heated infinite vertical plates, and, in particular, predicted values of the wave speed for travelling instabilities on the thermal boundary layer. The analysis is, however, based on the assumption of a stable background stratification in both the fluid and on the vertical plates, which is not the case for either group of travelling waves discussed here. In both cases, the background stratification has not been established at the time of passage of the instabilities. The zero-stratification-parameter results presented by Bergholz (for Pr values other than the present case) correspond to closely spaced plates, in which the boundary layers encompass the entire cavity, and are not applicable here.

Le Queré & Alziary de Roquefort (1986) observed similar travelling perturbations in a numerical simulation of convection in a rectangular cavity. In that case, a steady solution was disturbed by increasing the Rayleigh number instantaneously, and, for $Ra > 2.1 \times 10^6$ and $A > 2$ they observed waves which travelled up the boundary layer and across the intrusion to be entrained into the opposing boundary layer. Although these waves were not generated by either the flow initiation or the impact of the intrusion, they appear to be of similar character to those observed here.

The properties of such buoyancy-driven instabilities have been extensively studied (for example Gill & Davey 1969 and Tzuoo, Chen & Armaaly 1985, as well as Bergholz 1978) and further investigation is outside the scope of this paper. It is interesting to speculate, however, that these perturbations may play a role in the transition to turbulence observed in high-Ra flows of this kind. In the present case, the perturbations decay on the horizontal intrusion before the far wall is reached; in the Le Queré and Alziary de Roquefort (1986) case the perturbations survive the horizontal passage and a periodic quasi-steady flow is established. Numerical investigations by Paolucci & Chenoweth (1989) of a problem similar to that studied by Le Queré & Alziary de Roquefort indicated that at higher Ra values, chaotic flow results. One possible inference is that the perturbations evident in the unsteady flow

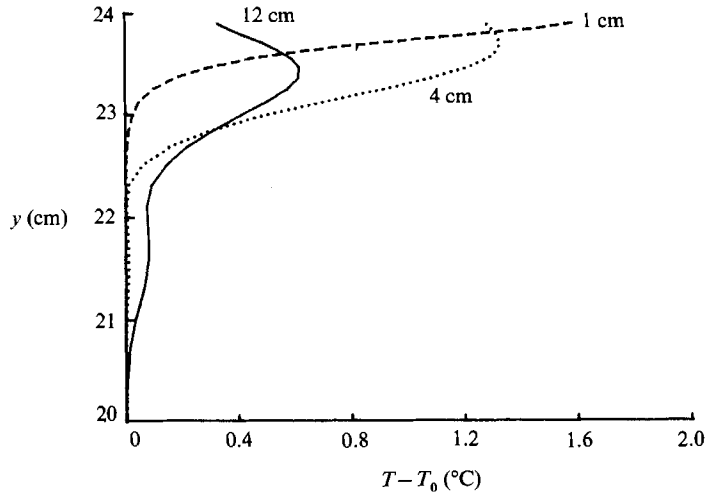

FIGURE 10. Computed temperature profiles across the heated intrusion at distances 1 cm, 4 cm, and 12 cm out from the hot wall, as shown.

described here will become unstable on both vertical and horizontal layers, with the possibility of a transition to locally chaotic flow at sufficiently high Rayleigh numbers.

The structure of the velocity field near the emerging intrusions is similar in general terms to that observed by Ivey (1984), and to the simulations of Schladow *et al.* (1989). While the concept of an internal hydraulic jump is attractive, there are several features which suggest that other mechanisms may be responsible. Following Ivey's scaling for the Froude number of the exiting flow, a value of O (4) is suggested for the present case. Further, using the PI scaling for velocity and intrusion thickness yields a Reynolds number $Re \sim Ra^{\frac{1}{4}}/Pr$, which for the present case is O (20). These values suggest that the flow structure will be quite laminar, but that if the structure is indeed an internal jump, significant entrainment should occur. Ivey associated this entrainment with the temperature fluctuations measured in the intrusion. These fluctuations have also been observed and simulated in the present case, arising from the perturbations generated on the thermal boundary layer, quite independently of the flow structure in the intrusion. Further, Paolucci & Chenoweth (1989) gave values, based on their simulations, of the order of magnitude constants associated with the steady-state Froude-number calculations; for this flow the Paolucci & Chenoweth constants yield an internal Froude number of 0.3, much less than that required for the presence of a jump. Based on the present simulations, the calculation of mean velocity and temperature fields over the width of the intrusion, upstream of the rapid flow divergence, yields a maximum Froude number of 0.7, from the unsteady part of the flow. In both cases, the implication is that the flow is subcritical on exit from the corner, and that the rapid flow divergence observed is due to other mechanisms.

Reference to figure 5 clearly shows the formation of the flow divergence downstream of the emerging intrusion. At $t = 80$ s (figure 5*d*) for example, the region of divergence is established in the region 2 to 8 cm in from the corner; beyond 8 cm, the flow has returned to the wall although the intrusion is much broader. Figures 10 and 11 show the computed temperature and horizontal velocity profiles in the region of the upper horizontal boundary at $t = 80$ s, for horizontal locations before the

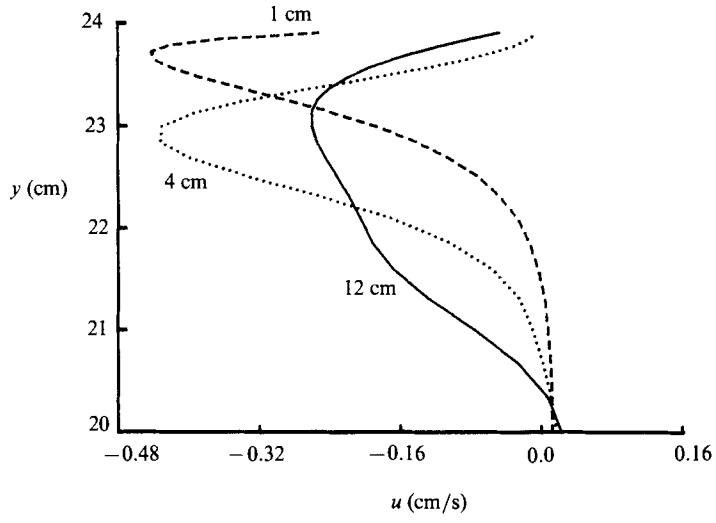

FIGURE 11. Computed horizontal velocity profiles across the heated intrusion, at the same locations used in figure 10.

divergence (1 cm away from the corner), in the midst of the divergence (4 cm) and after the flow has returned to the wall (12 cm). Observation of these profiles gives rise to the formulation of an hypothesis for the mechanism responsible for the divergence.

Consider the temperature profiles first. On exit from the corner, the temperature profile retains the characteristics of the vertical-wall thermal boundary; that is, a very rapid reduction in temperature over a scale of 0.5 cm. As the vertical wall provided a source of heat, this is consistent with the thermal boundary condition on that wall. However, it is not consistent with the insulated condition on the horizontal wall, and the profile must adjust to provide a zero gradient normal to the wall. As no heat can escape through the wall, this is only possible if heat is transferred towards the centre of the cavity. This means that the temperature at the horizontal boundary will decrease, and the temperature for some region interior to the boundary will increase, over the original values. The profile at 4 cm in from the corner shows this characteristic, further distorted by convection. The convective effect is present as $Pr > 1$, and the velocity peak is further removed from the boundary than the influence of the thermal boundary adjustment. Between the point at which the profiles cross and the wall the fluid is cooler than the incoming stream; beyond the crossover, the fluid is warmer. There will therefore be a blocking effect at this point, with a tendency for the intrusion to split around the crossover point. However, the location of the crossover is determined by thermal conduction, and its position moves out from the horizontal boundary following the usual $(\kappa t)^{\frac{1}{2}}$ law, beginning immediately the flow turns the corner. The net effect is that the intrusion diverges immediately, and separates from the wall. With a Reynolds number of O (20), inertia is dominant, and the flow retains a coherent jet-like structure until viscosity becomes important. Following PI, this occurs in time T_t, where

$$T_t \sim \frac{h^2}{\kappa Pr^{\frac{5}{3}} Ra^{\frac{1}{3}}}. \tag{16}$$

For the present case, $T_t \sim 20$ s, and with the PI-scale velocity in an inertial intrusion

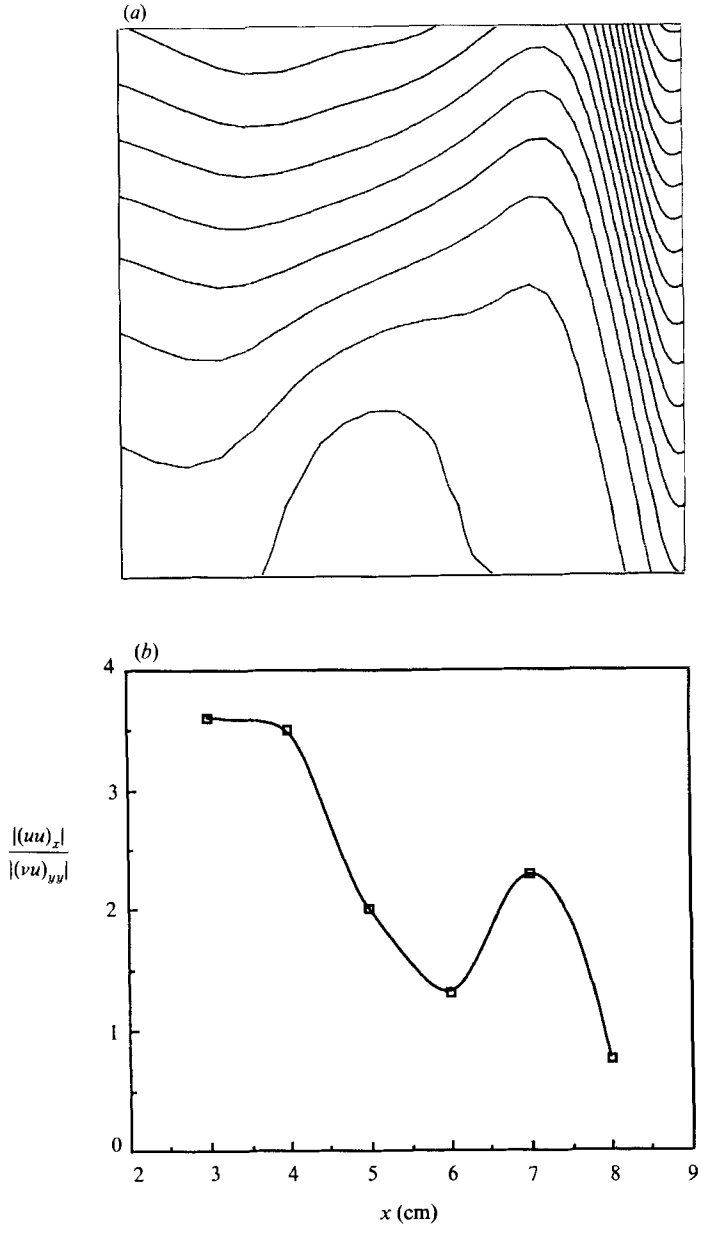

FIGURE 12. (*a*) The computed pressure contours in the region of the emergent corner. (*b*) The ratio of the vertically integrated inertial and viscous terms in the horizontal momentum equation in the same region as (*a*), from the simulation results.

of O (3 mm s^{-1}), the intrusion will begin to spread back towards the boundary at a distance O (6 cm) in from the emergent corner. Both experimental and numerical results show (figure 5*d*) the jet diverging at a distance of approximately 6 cm in from the corner.

The numerical results may be used to confirm in detail the above mechanism. figure 12(*a*) shows the simulated pressure contours in the region of the emergent hot

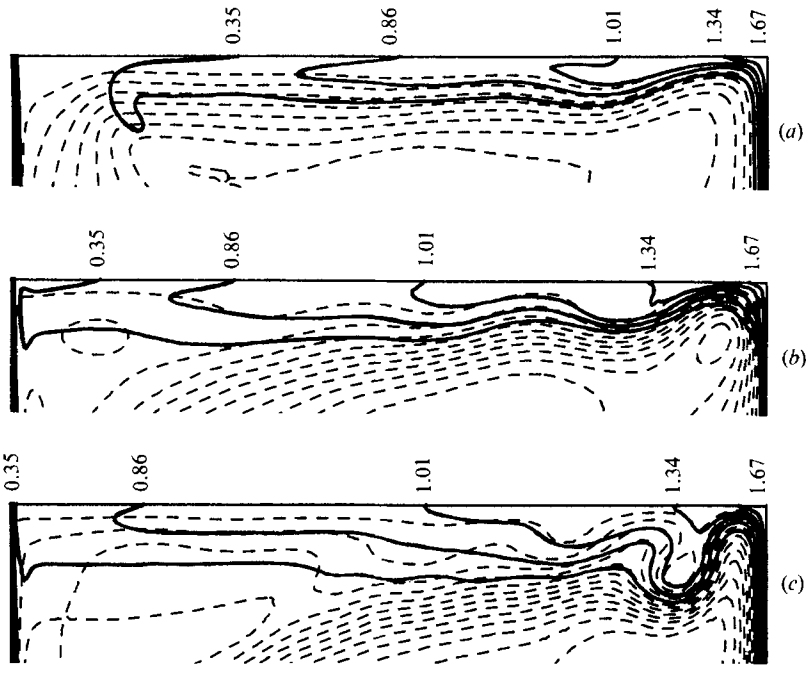

FIGURE 13. The computed streamlines (broken lines) and temperature contours (solid lines) describing the heated intrusion and its impact on the far-wall boundary layer, at times (*a*) $t = 100$ s, $\psi_{max} = 1.25 \times 10^{-3}$ m^2 s^{-1}; (*b*) $t = 167$ s, $\psi_{max} = 9.8 \times 10^{-4}$ m^2 s^{-1}; (*c*) $t = 232$ s, $\psi_{max} = 8.0 \times 10^{-4}$ m^2 s^{-1}. The temperature contours are at the values of $(T - T_0)$ °C shown, and the streamline contours are equally spaced between the boundary value (zero) and the maximum value indicated.

intrusion. The high-pressure region located against the horizontal wall is the result of the horizontal gradient in temperature referred to above. In figure 12(*b*), the value of the ratio of the inertial and viscous terms of the horizontal momentum equation, averaged across the intrusion thickness, is shown. Clearly the inertial terms dominate in the region upstream of the peak divergence from the boundary at 6 cm from the corner; downstream of that point the terms are of similar order.

The splitting of the intrusion at the far end as it impacts the opposing wall has an important effect on both the subsequent behaviour of the flow divergence just discussed, and on the progression to steady state. Again, the simulation results are used to examine this mechanism in detail. Figure 13(*a*) shows the simulated streamline and temperature contours in the upper half of the cavity at time $t = 100$ s, indicating that approximately half of the intrusion contains fluid from the core region at ambient temperature, consistent with the knowledge from above that, at this stage, the intrusion is governed by a viscous–buoyancy balance. At time $t = 167$ s (figure 13*b*), the intrusion has hit the wall. The streamline pattern in the region of the impacting corner has changed character considerably, with a clear indication of a divergence of the flow into two streams; the first, comprising the heated fluid, along the horizontal wall, and the second, comprising the fluid at ambient temperature, into the core region, away from the corner. An enlargement of the corner region at time $t = 167$ s (figure 14) indicates that there is recirculation in the split region. As time increases, the split region moves back towards the emergent corner and at $t = 232$ s (figure 13*c*), has penetrated sufficiently far to influence the

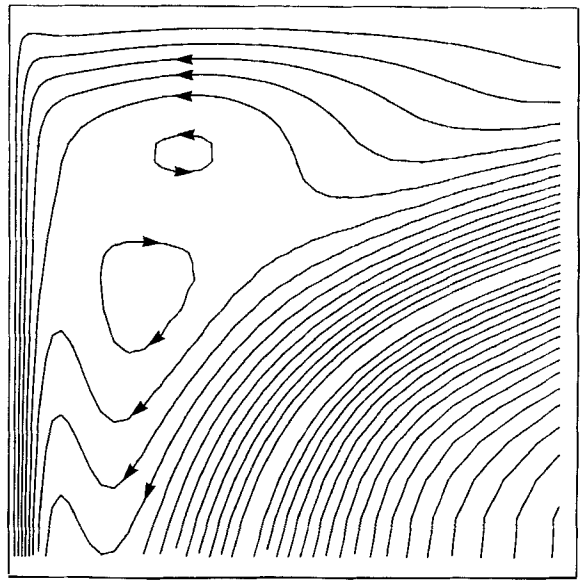

FIGURE 14. The computed streamlines in the region of the interaction between the intrusion and the far-wall boundary layer, at time $t = 167$ s. The streamline contours are equally spaced between the boundary value (zero) and $\psi_{max} = 1.0 \times 10^{-3}$ m^2 s^{-1}.

divergent flow structure at that location. A detailed examination of the complex interaction between the splitting and the divergent flow is beyond the scope of this paper; qualitatively, the effect is to force the divergent flow back towards the emergent corner as observed in figure 5.

The mechanism for the splitting of the intrusion is related to that proposed by PI for the generation of the cavity-scale internal waves. Briefly, the far-wall boundary layer entrains fluid over its full length and is unable to entrain the incoming intrusion over the intrusion thickness alone, as postulated by PI, and some backflow is inevitable. Since the intrusion is stratified, the heated backflow will intrude between the incoming heated fluid and the ambient-temperature fluid, generating the splitting as shown.

6. Conclusions

In this paper an experimental and numerical programme to investigate the development of the flow arising from the application of an instantaneous heating and cooling of the opposing sidewalls of a square cavity has been described. The experimental apparatus ensured that the start up was virtually instantaneous, and frequent streak photographs have given a good description of the flow. The flow showed several general features similar to the only other relevant experimental result, but was significantly different in detail. In particular, although the structure near the emerging horizontal hot and cold intrusions was similar to that observed by Ivey (1984), an alternative mechanism to the internal hydraulic jump suggested by Ivey has been proposed.

The numerical results were compared with the experimental results at two levels. First, a sequence of streak photographs were compared with instantaneous streamline plots from the numerical simulation, and in general, the numerical results

reproduced the features of the flow. At a more quantitative level, thermistor time series from the experiment were compared with the simulated temperature time series at the same points. These results were extremely sensitive to the location of the thermistors and the simulation points as the temperature gradient in this region was high; the comparison, however, revealed that the features of the experimental results were reproduced by the simulation, with a small timing offset. In particular, the presence and character of the two separate occurrences of boundary-layer instability are reproduced accurately by the simulation.

The high-frequency signal observed in the thermistor time series recorded here is of similar character to that observed by Ivey. In this case, however, it has been demonstrated that this is the result of the passage of the boundary-layer perturbations along the intrusions, rather than the downstream effects of an internal hydraulic jump as suggested by Paolucci & Chenoweth (1989) for the Ivey experiment. The Chenoweth & Paolucci (1986) calculations for Froude number would generate internal Froude numbers substantially less than unity for the present and other lower-Ra cases which, at least numerically, show an indication of the oscillatory behaviour. Based on the present numerical results, the Froude number is also less than unity. Further, many of the numerical cases treated by PI gave an indication of highly damped oscillatory behaviour, but with no evidence of the complex flow structures near the emerging intrusions. This suggests that the low-frequency oscillatory behaviour is related to mechanisms other than the formation of the flow divergence near the emergence of the intrusions. The high-frequency signal modulating the Nusselt-number plots is the result of the boundary-layer perturbations being advected across the cavity. It is possible that these are responsible for transition to turbulence at higher Rayleigh numbers when the perturbations become chaotic on the boundary layer or on the intrusion. It also appears possible that the periodic flows simulated by Le Queré & Alziary de Roquefort (1986) arise from these perturbations travelling around the cavity. Although modified by the presence of the flow divergence, these perturbations are not produced by the emerging intrusions.

The other aspect of interest from the Ivey (1984) experiments was the presence of the counter-rotating core motion. There was no evidence of this in the present experiments, supporting the conclusions of Schladow *et al.* (1989). The presence of cavity-scale internal waves was observed; however, the amplitude of the oscillation in the temperature signals is small. In common with the Ivey result the oscillation was therefore not readily evident in the temperature signal in the intrusion; however, the difference between the two signals gives strong evidence of the oscillatory nature after the other features (for example the travelling instabilities) had passed. Although the amplitude was weak, the integrated nature of the computed Nusselt numbers shows the oscillation clearly.

Several features therefore emerged as crucial to an understanding of the transient features of the flow. These were the development of the boundary-layer instabilities, the formation of the rapid flow divergence near the emerging intrusion corner, the splitting of the intrusion on impact with the far vertical wall, and the related presence of low-frequency signals in the temperature and Nusselt number. Although some discussion of each of these aspects has been presented, a full analysis is outside the scope of this paper. However, some details have been presented. In particular, the presence of the perturbations has been discussed in the light of both the experimental and numerical results, a mechanism for the formation of the rapid flow divergence suggested, the splitting of the intrusion placed in the context of the

previous PI result, and the presence of the internal waves is strongly supported. These aspects are presently being pursued in more detail.

The authors thank Jorg Imberger and Greg Ivey for their useful suggestions. Rosa Villani assisted with the experimental work. The authors also thank Geoff Schladow for making available a prepublication copy of Schladow (1990). This research was supported by the Australian Research Council, a National Research Fellowship and the Australian Water Research Advisory Council.

REFERENCES

ARMFIELD, S. W. 1989 Direct simulation of unsteady natural convection in a cavity. In *Proc. 3rd Intl Symp. on Computational Fluid Dynamics, Nagoya*, pp. 305–310. North-Holland.

BATCHELOR, G. K. 1954 Heat transfer by free convection across a closed cavity between vertical boundaries at different temperatures. *Q. J. Appl. Maths* **12**, 209–233.

BERGHOLZ, R. F. 1978 Instability of steady natural convection in a vertical fluid layer. *J. Fluid Mech.* **84**, 743–768.

BROWN, S. N. & RILEY, N. 1973 Flow past a suddenly heated vertical plate. *J. Fluid Mech.* **59**, 225–237.

CARSLAW, H. A. & JAEGER, J. C. 1959 *Conduction of Heat in Solids*. Oxford University Press.

CATTON, I. 1978 Natural convection in enclosures. *6th Intl Heat Transfer Conf. Toronto*, vol. 6, pp. 13–43. Hemisphere.

CHENOWETH, D. R. & PAOLUCCI, S. 1986 Natural convection in an enclosed vertical air layer with large horizontal temperature differences. *J. Fluid Mech.* **169**, 173–210.

GEBHART, B. & MAHAJAN, R. L. 1982 Instability and transition in buoyancy induced flows. *Adv. Appl. Mech.* **22**, 231–315.

GILL, A. E. & DAVEY, A. 1969 Instabilities of a buoyancy-driven system. *J. Fluid Mech.* **35**, 775–798.

GRESHO, P. M., LEE, R. L., CHAN, S. T. & SANI, R. L. 1980 Solution of the time-dependent incompressible Navier–Stokes and Boussinesq equations using the Galerkin finite element method. In *Approximation Methods for Navier–Stokes Problems* (ed. R. Rautmann). Lecture Notes in Mathematics vol. 771, pp. 203–222. Springer.

ISSA, R. I. 1983 Solution of the implicitly discretised fluid flow equations by operator splitting. *Rep.* FS/82/15. Imperial College London.

IVEY, G. N. 1984 Experiments on transient natural convection in a cavity. *J. Fluid Mech.* **144**, 389–401.

JACKSON, C. P. & ROBINSON, P. C. 1985 A numerical study of various algorithms related to the preconditioned conjugate gradient method. *Intl J. Num. Methods Engng* **21**, 1315–1338.

KIGHTLY, J. R. 1986 The conjugate gradient method applied to turbulent flow calculations. In *Proc. 6th GAMM Conf. on Numerical Methods in Fluid Mechanics* (ed. D. Rues & W. Kordulla), pp. 161–168.

LEONARD, B. P. 1979 A stable and accurate convective modelling procedure based on quadratic upstream interpolation. *Comput. Meth. Appl. Mech. Engng* **19**, 59–98.

LE QUERÉ, P. & ALZIARY DE ROQUEFORT, T. 1985 Transition to unsteady natural convection of air in differentially heated vertical cavities. In *Numerical Methods in Laminar and Turbulent Flow, Proc. 4th Intl Conference, Swansea*, pp. 841–852.

MALISKA, C. R. & RAITHBY, G. D. 1983 Calculating 3-D fluid flows using non-orthogonal grid. In *Proc. Third Intl Conf. on Numerical Methods in Laminar and Turbulent Flows, Seattle*, pp. 656–666. Pineridge.

OSTRACH, S. 1982 Natural convection heat transfer in cavities and cells. *7th Intl Heat Transfer Conf. Munich*, vol. 1, pp. 365–379. Hemisphere.

PAOLUCCI, S. & CHENOWETH, D. R. 1989 Transition to chaos in a differentially heated vertical cavity. *J. Fluid Mech.* **201**, 379–410.

PATANKAR, S. V. 1980 *Numerical Heat Transfer and Fluid Flow*. Hemisphere.

PATTERSON, J. C. 1983 General derivative approximations for finite difference schemes. *Intl J. Numer. Meth. Engng* **19**, 1235–1241.

PATTERSON, J. C. 1984 On the existence of an oscillatory approach to steady natural convection in cavities. *Trans. ASME* C: *J. heat Transfer* **106**, 104–108.

PATTERSON, J. C. 1989 Experiments in unsteady natural convection. In *Proc. Fourth Australasian Conference on Heat and Mass Transfer, Christchurch*, pp. 299–306.

PATTERSON, J. C. & IMBERGER, J. 1980 (referred to herein as PI). Unsteady natural convection in a rectangular cavity. *J. Fluid Mech.* **100**, 65–86.

PERNG, C. Y. & STREET, R. L. 1990 Three dimensional unsteady flow simulations: alternative strategies for volume averaged calculation. *Intl J. Numer. Meth. Fluids* (in press).

RHEE, H. S., KOSEFF, J. R. & STREET, R. L. 1984 Flow visualization of a recirculating flow by rheoscopic liquid and liquid crystal techniques. *Exps. Fluids* **2**, 57–64.

SCHLADOW, S. G. 1990 Oscillatory motion in a side-heated cavity. *J. Fluid Mech.* **213**, 589–610.

SCHLADOW, S. G., PATTERSON, J. C. & STREET, R. L. 1989 Transient flow in a side-heated cavity at high Rayleigh number: a numerical study. *J. Fluid Mech.* **200**, 121–148.

STAEHLE, B. & HAHNE, E. 1982 Overshooting and damped oscillations of transient natural convection flows in cavities. *7th Intl Heat Transfer Conf., Munich*, vol. 2, pp. 287–292. Hemisphere.

TZUOO, K. L., CHEN, T. S. & ARMAALY, B. F. 1985 Wave instability of natural convection flow on inclined surfaces. *Trans. ASME* C: *J. Heat Transfer* **107**, 107–111.

VAN DOORMAL, J. P. & RAITHBY, G. D. 1984 Enhancements of the SIMPLE method for predicting incompressible fluid flows. *Numer. Heat Transfer* **9**, 147–163.

YEWELL, P., POULIKAKOS, D. & BEJAN, A. 1982 Transient natural convection experiments in shallow enclosures. *Trans. ASME* C: *J. Heat Transfer* **104**, 533–538.